



**Environmental
Science**
Nano

**One-step Biosynthesis of Bilayered Graphene Oxide
Embedded Bacterial Nanocellulose Hydrogel for Versatile
Photothermal Membrane Applications**

Journal:	<i>Environmental Science: Nano</i>
Manuscript ID	EN-ART-08-2021-000754.R1
Article Type:	Paper

SCHOLARONE™
Manuscripts



Double-Anonymised Title Page

One-step Biosynthesis of Bilayered Graphene Oxide Embedded Bacterial Nanocellulose Hydrogel for Versatile Photothermal Membrane Applications

Authors:

*Govindaraj Divyapriya,^{ab} Asifur Rahman,^{ab} Weinan Leng,^{ab} Wei Wang,^{ab} and Peter J. Vikesland^{*ab}*

Affiliations:

a Department of Civil and Environmental Engineering, Virginia Tech, Blacksburg, Virginia, USA

b Virginia Tech Institute of Critical Technology and Applied Science (ICTAS), Sustainable Nanotechnology Center (VTSuN), Blacksburg, Virginia, USA

Acknowledgements:

This research was supported by the Fulbright Program, United States-India Educational Foundation, India, and Institute of International Education, USA (2471/FNPDR/2019) and NSF PIRE grant (479477). Laboratory and instrumentation support was provided by Virginia Tech Institute of Critical Technology and Applied Science (ICTAS) Sustainable Nanotechnology Center, Blacksburg, USA.

Author contributions:

G. Divyapriya directed the research effort, wrote the manuscript, and provided oversight of the remainder of the research team.

A. Rahman, W. Leng, and W. Wang provided experimental results and aided in the writing of the manuscript.

P. Vikesland obtained research funding, provided oversight of the project, and collaborated in writing and editing of the manuscript.

All authors contributed to the development of the manuscript and its revision.

One-step Biosynthesis of Bilayered Graphene Oxide Embedded Bacterial Nanocellulose Hydrogel for Versatile Photothermal Membrane Applications

Environmental significance

The sustainability capacity of the developing world is being stressed by the ever-increasing demand for clean water and energy resources. Efficient tapping of abundance solar energy to harvest clean water is the viable solution to the world's problem at water-energy nexus. Developing a nano-enabled photothermal membranes are a way forward towards sustainable water purification through filtration, photothermal disinfection and distillation. Layered integration of desired functions of photothermal materials onto the suitable support material without compromising its chemical, thermal and mechanical properties remain challenging. In this study, firstly we demonstrated a one-step green approach to biosynthesize the bilayer structured hydrogel composite of graphene oxide (GO) and bacterial nanocellulose (BNC) through modifying the growth rate of BNC producing bacteria *Gluconacetobacter xylinus*. The *in-situ* integration of GO layers onto the BNC fiber network was controlled via amending the corn steep liquor as bacterial growth enhancer. Multipurpose nature of the biosynthesized photothermal membranes were explored.

Abstract

We introduce the facile one-step biosynthesis of a bilayer structured hydrogel composite of reduced-graphene oxide (rGO) and bacterial nanocellulose (BNC) for multiple photothermal water treatment applications. One-step *in-situ* biosynthesis of bilayered hydrogel was achieved via modification of BNC growth medium supplemented with an optimized concentration of corn steep liquor as growth enhancer. A two-stage, growth rate-controlled formation mechanism for the bilayer structure was revealed. The final cleaned and freeze-dried reduced-GO embedded BNC bilayer membrane enables versatile applications such as filtration (tested using gold nanoparticles, *Escherichia coli* cells (*E. coli*), and plasmid DNA), photothermal disinfection of entrapped *E. coli*, and solar water evaporation. Comparable particle rejection (up to ≈ 4 nm) and water flux ($146 \text{ L h}^{-1} \text{ m}^{-2}$) to ultrafiltration was observed. Entrapment and photothermal inactivation of *E. coli* cells was accomplished within 10 mins of solar exposure (one sun). Such treatment can potentially suppress membrane biofouling. Steam generation capacity was $1.96 \text{ kg m}^{-2} \text{ h}^{-1}$. Our simple and scalable approach opens a new path for biosynthesis of nanostructured materials for environmental and biomedical applications.

Keywords: Photothermal membrane; graphene oxide; bacterial nanocellulose; solar water treatment; photothermal disinfection; solar steam generation

1. Introduction

Solar driven water treatment processes are gaining tremendous attention owing to the global water crisis.¹ Photothermal water treatment processes provide opportunities to develop low cost, decentralized, modular, and integrative approaches to produce clean water in resource-limited regions.² Photothermal materials that efficiently absorb and convert the broad electromagnetic spectrum of incident sunlight into thermal energy can be designed and applied for targeted treatment.^{1,3} Exemplary photothermal approaches include bacterial inactivation to control biofouling in reverse osmosis/ultrafiltration membranes, photothermal evaporation/distillation, and hybrid photothermal-photocatalysis processes.^{2,4-7} A range of inorganic metals and metal oxides and carbon nanomaterials have been reported for their high light-to-heat conversion efficiencies.^{1,3} Metal and semiconductor-based photothermal materials include Au and Ag nanostructures,⁸ molybdenum disulfide,⁹ titanium oxides,^{10,11} and MXenes.¹² Similarly, carbon-based materials including nanocarbon and polymeric materials such as carbon black,¹³ graphene (GO) or reduced graphene oxide (rGO),¹⁴ carbon nanotubes,¹⁵ polydopamine,¹⁶ and polypyrrole have been proposed.¹⁷ Graphene is considered one of the more interesting and low-cost 2D materials as it possesses excellent electrical, optical, thermal, photothermal, and mechanical properties.¹⁸ GO absorbs visible and near-infrared light across a broad electromagnetic spectrum.^{2,19,20} Due to electron excitation and the relaxation of loosely bound π electrons the conversion of incident light into heat occurs efficiently.^{2,19,20} Photothermally active graphene-

1
2
3 based thin film membranes minimize biofouling and selectively transport ions/molecules; while
4
5 graphene-based thick foams generate steam and harvest clean water via distillation.^{2,14,21}
6
7

8
9 Graphene based membranes have been shown to demonstrate high water permeability and precise
10
11 sieving ability.²² However, the stability and durability of free-standing graphene/GO laminates are
12
13 compromised for large-scale application due to the damage that can occur during operation.^{14,23}
14

15
16 Several porous polymeric supporting materials such as polysulfone,²⁴ polyethersulfone,²⁵
17
18 poly(vinylidene fluoride),²⁶ and polyvinyl alcohol²⁷ are being explored to improve water
19
20 permeability as well as the chemical and mechanical stability of graphene/GO-based membranes.
21

22
23 Similarly, the use of graphene-based foams for solar evaporation processes requires three-
24
25 dimensional porous bilayered materials consisting of a photothermal layer supported by a more
26
27 rigid thermal insulation layer.^{3,21} The photothermal layer absorbs broad-spectrum light while
28
29 creating a localized heating interface for conversion of light into heat;^{28,29} whereas the low thermal
30
31 conductivity insulation layer increases water transport to the evaporation surface and minimizes
32
33 heat transfer to bulk water.^{3,21} Inexpensive low thermal conductivity supporting materials used as
34
35 insulation layers for solar steam generation, including the non-carbohydrate polymer (lignin made
36
37 by monomers of monolignols, p-coumaryl alcohol, coniferyl alcohol, and sinapyl alcohol)³⁰ and
38
39 carbohydrate polymer (cellulose containing glucose as the monosaccharide unit)³¹ based material
40
41 such as cotton,³² wood,^{33,34} bamboo,³⁵ and bacterial nanocellulose (BNC).²¹
42
43
44
45

46
47 BNC is extremely promising for the development of engineered materials owing to its high surface
48
49 area, microporous nature, tensile and mechanical strength, and its facile biosynthesis and low
50
51 environmental footprint.³⁶⁻³⁹ Biosynthesis of BNC by bacteria within the *Gluconacetobacter*
52
53 genus is widely reported.³⁸ These bacteria produce extracellular cellulose nanofibers that
54
55 intertwine to form a porous 3D network.^{40,41} Typically, the anchoring of graphene/GO sheets onto
56
57

1
2
3 supporting polymers such as cellulose is carried out through techniques that include vacuum
4 deposition and layer by layer assembly.^{42–44} Some researchers, however, have reported synthesis
5 of a GO embedded BNC membrane via external incorporation of GO onto pre-synthesized BNC
6 by vacuum filtration.^{42,43} Unfortunately, the long-term chemical and mechanical stabilities of these
7 membranes are insufficient.¹⁴ Promisingly, the *in-situ* incorporation of GO sheets within the BNC
8 fiber networks during the growth of *Gluconacetobacter* has led to increased structural integrity
9 and stability of the composite membrane.^{45–47} The incorporation of GO sheets within entangled
10 BNC fibers occurs following the initial adsorption of GO sheets and subsequent biosynthesis of
11 the BNC fibers.^{45–47} In-situ biosynthesis of spherical structured GO/BNC hydrogel was reported
12 using a dynamic cultivation route.^{48,49} Whereas the membrane like structures are obtained with the
13 static cultivation method.^{14,21} Microbial growth kinetics of *in-situ* biosynthesis of rGO/BNC
14 hydrogel and the analysis of percolated network formation are detailed by Dhar et al.⁵⁰
15 Incorporation of GO/rGO nanosheets into the intergalleries of BC nanofibers occurs through
16 hydrogen bonding interactions and the growth kinetics were controlled by the carbon substrate as
17 well as oxygen at the air-media interface.⁵⁰ Applications of GO embedded BNC based
18 photothermal membranes for efficient biofouling-controlled ultrafiltration and solar steam
19 generation processes were recently reported by Jiang et al.^{14,21}
20
21
22
23
24
25
26
27
28
29
30
31
32
33
34
35
36
37
38
39
40
41
42

43 Jiang et al. introduced²¹ a two-step bilayer production of GO embedded BNC hydrogel where a
44 pristine BNC layer was grown by adding nutrient medium on top of a previously prepared
45 GO/BNC hydrogel. The present study was conducted to (i) demonstrate reproducible single-step
46 production of bilayer membranes, and (ii) evaluate the utility of these bilayer membranes for
47 versatile applications including filtration, photothermal disinfection, and steam generation. We
48 developed a simple and novel, single-step biosynthesis by altering the growth medium through
49
50
51
52
53
54
55
56
57
58
59
60

1
2
3 supplementation of corn steep liquor (CSL) as growth enhancer. The influence of the composition
4 of the growth medium (at different concentrations of growth substrate and GO mixtures) on *in-*
5
6 *situ* formation of BNC and the subsequent incorporation of GO to the BNC fibers has not been
7
8 previously evaluated. We hypothesized that (i) *in-situ* integration of GO sheets within the growing
9
10 BNC fiber matrix could be controlled by altering the growth rate of *Gluconacetobacter xylinus* (*G.*
11
12 *xylinus*) and that (ii) bilayer formation of the hydrogel (GO embedded BNC layer and subsequent
13
14 pristine BNC layer) in a single step occurs via control of two growth rate-based stages that occur
15
16 during the incubation period. The following assessments were performed: (i) to evaluate the role
17
18 of CSL as a growth enhancer for BNC growth rate modification, (ii) to reveal the growth rate
19
20 controlled attachment of GO to the BNC fibers, (iii) to optimize CSL supplement and GO loading
21
22 in the growth medium to obtain a bilayer structured hydrogel with the desired biomass, (iv) to
23
24 assess filtration performance for the desired flux and particle rejection, (v) to study the
25
26 photothermal inactivation of entrapped bacteria, and (vi) to evaluate water evaporation from the
27
28 bilayer membrane.
29
30
31
32
33
34
35

36 **2. Materials and methods**

37 **2.1. Materials**

38
39
40
41 GO (0.4 wt%, monolayer content >95%) was purchased from MSE Supplies (Tucson, USA).
42
43 Fructose (>99%), yeast extract, corn steep liquor (CSL), magnesium sulfate (MgSO_4 , $\geq 99.5\%$),
44
45 potassium dihydrogen phosphate (KH_2PO_4 , 99.995%), sodium hydroxide (NaOH , $\geq 97.0\%$), and
46
47 hydrochloric acid (HCl , 37%) were procured from Sigma-Aldrich, USA. All experiments were
48
49 carried out using deionized water with a resistance $\geq 18 \text{ M}\Omega \text{ cm}$.
50
51
52
53

54 **2.2. Production of bilayered rGO embedded BNC membranes**

1
2
3 *G. xylinus* (ATCC® 10245™) was employed to produce bacterial nanocellulose fibers. A dense
4 suspension of *G. xylinus* was cultured using a growth medium composed of 40 g fructose, 5 g yeast
5 extract, 0.25 g MgSO₄, and 1 g KH₂PO₄ dissolved in 1 L deionized water. Dense bacterial cultures
6 were obtained by inoculating 1 mL of *G. xylinus* (~10⁵ CFU/mL) in 100 mL of growth medium
7 and then incubating at 37 °C for 3 days at 150 rpm in a shaker incubator. During incubation,
8 nascent BNC pellicles developed at the air-liquid interface. At the conclusion of the incubation
9 period, the cultured flask along with the BNC pellicle was vigorously shaken using a vortex shaker
10 at 3200 rpm for 5 min to detach the bacteria from the BNC pellicle into the liquid medium. This
11 suspension was used as pre-culture (~ 10⁸ – 10⁹ CFU/mL) in further experiments.
12
13
14
15
16
17
18
19
20
21
22
23

24 To study the influence of the CSL bacterial growth enhancer on the production of bilayered
25 hydrogel, the growth medium was modified by addition of varying concentrations of CSL (0, 20,
26 40, 60, 80 mL of CSL per L of growth medium) to a fixed GO concentration of 0.05 w/v %. The
27 modified growth media were inoculated with pre-cultured *G. xylinus* at 0.1 v/v %. The prepared
28 mixtures, with volume 20 mL, were poured into disposable Petri dishes (100 mm diameter, 15 mm
29 deep) and incubated at 37 °C for 72 h under aerobic and static conditions. To further optimize GO
30 loading onto the bilayered hydrogel, the growth media were modified with varied concentrations
31 of GO (0.025, 0.05, 0.075 wt/v %) at a fixed CSL supplementation of 20 mL/L and 0.1 v/v % of
32 pre-culture. The GO embedded BNC hydrogels were boiled with 0.2 M NaOH for 1 h to eliminate
33 attached bacteria and residual nutrient media. This process is known to result in the partial
34 reduction of GO.¹⁴ Cleaned hydrogels were then washed with deionized water for 48 h with
35 periodic change of water. The purified hydrogels were freeze-dried for 24 h to acquire single-
36 layered (rGO/BNC) and bilayered (rGO/BNC:BNC) membranes. Changes in the production of
37 GO/BNC for different CSL and GO supplementations are listed in Table 1.
38
39
40
41
42
43
44
45
46
47
48
49
50
51
52
53
54
55
56
57
58
59
60

Table 1. Summary of single-layered (rGO/BNC) and bilayered (rGO/BNC:BNC) membranes produced in the different growth mediums.

Membrane ID	CSL (mL/L)	GO Loading (wt/v%)	Weight of hydrogel (g)	Dry weight (g)
M0	0	0.05	7.43 ± 0.68	0.022 ± 0.0019
M1/G2	20	0.05	12.73 ± 0.14	0.057 ± 0.0047
M2	40	0.05	13.28 ± 0.53	0.083 ± 0.0070
M3	60	0.05	15.31 ± 0.58	0.108 ± 0.0043
M4	80	0.05	17.87 ± 0.66	0.133 ± 0.0013
G0	20	0	14.05 ± 0.71	0.091 ± 0.0022
G1	20	0.025	11.36 ± 0.25	0.06 ± 0.0049
G3	20	0.075	13.11 ± 0.47	0.07 ± 0.0018

2.3. Membrane characterization

Surface morphology and cross-sectional analysis of the membranes were performed using a Quanta 600 FEG environmental SEM with the operating voltage of 3 kV. Nonconductive BNC samples were sputter-coated with iridium before the analysis, while the conductive rGO/BNC membranes were directly analyzed without sputter coating. GO dispersion in ethanol (0.04 mg/mL) was drop-cast on the Si substrate for the SEM analysis. The chemical nature of the GO/rGO within the BNC membrane was probed using X-ray photoelectron spectroscopy (XPS). XPS spectra were collected using a PHI Quantera SXM (ULVAC-PHI, Japan) with a hemispherical energy analyzer and a monochromatic aluminum target. Survey spectra were collected at 25 W/15 kV with a spot size of 100 μm, 45° take-off angle, and 280 eV pass energy. A 69 eV pass energy with a 0.125 eV scan step were chosen for high resolution spectrum acquisition. To quantify the extent of GO anchoring to BNC, thermogravimetric analysis (TGA) was performed over the temperature range of 25-700 °C using a TA instrument-TGA5500 with a

1
2
3 heating rate of 10 °C min⁻¹ under nitrogen atmosphere. Raman analysis of the GO was performed
4 using a WITec alpha 500R Raman spectrometer (785 nm laser; WITec GmbH, Ulm, Germany).
5
6 The bilayer structure of the membrane was analyzed through digital photography using the 100×
7
8 Olympus objective lens of the Raman microscope.
9
10

11 12 13 **2.4. Filtration**

14
15
16 Membrane filtration performance was determined using gold nanoparticles (AuNPs synthesized
17 via citrate reduction;⁵¹ average diameters of ≈4.2 nm (44.8 nmol/L) and ≈20.6 nm (1.93 nmol/L)
18 as well as plasmid DNA (70 ng/mL). A dead-end filtration set-up was used for the filtration
19 experiments (8200 Ultrafiltration Stirred Cell, Millipore Corporation) as explained in Breazeal *et*
20 *al*⁵². The suspensions of AuNPs with volumes of 10-25 mL were loaded into the stirred cell. All
21 filtration experiments were carried out with an applied pressure of 30 psi; the pressure was
22 developed and controlled through the supply of nitrogen gas with a pressure regulator. Permeate
23 water flux was estimated based on the volume of filtrate collected per unit area of membrane per
24 unit time. As-synthesized AuNPs and their removal efficiency by filtration were analyzed using a
25 Cary 5000 UV–Vis–NIR spectrophotometer. To quantify plasmid DNA filtration, overnight
26 *Escherichia coli* cultures of 100 mL (inoculated with 1 mL of ~10⁶ CFU/mL) were used for the
27 extraction of double-stranded (ds) plasmid DNA and extracted using E.Z.N.A. plasmid DNA maxi
28 kit (D6922-02). The DNA concentration was analyzed using a Qubit 2.0 fluorometer (Invitrogen,
29 Thermo Fisher Scientific) and the Qubit dsDNA HS assay kit. The particle size of the AuNPs and
30 hydrodynamic diameter of the ds plasmid DNA was analyzed using dynamic light scattering (DLS)
31 with a Nano ZS instrument (Malvern Corporation, Malvern, UK).
32
33
34
35
36
37
38
39
40
41
42
43
44
45
46
47
48
49
50
51
52

53 54 **2.5. Photothermal disinfection**

1
2
3 Filtration followed by photothermal disinfection of *E. coli* bacteria was studied. An *E. coli*
4 suspension grown in LB broth was centrifuged at $3260 \times g$ (Thermo Scientific Sorvall ST 8
5 centrifuge) to remove residual medium and then rinsed twice with 1X phosphate-buffered saline
6 (PBS). *E. coli* cells ($\sim 2.0 \times 10^7$ CFU/mL) were suspended in PBS and used in filtration/
7 photothermal disinfection studies. An *E. coli* suspension of 10 mL was filtered through the
8 membranes to estimate their filtration efficiency. Collected filtrate was plated onto LB agar
9 medium via spread plating and then observed for bacterial colony formation for 24 h. Based on
10 the estimated CFU/mL, the filtration efficiency was calculated. Membranes with attached *E. coli*
11 were subsequently exposed to a solar simulator (Abet Technologies' Model 11002 SunLite,
12 Connecticut, USA) with an intensity of 0.6 KW/m^2 (one sun) and an exposure area of $50 \times 50 \text{ cm}^2$.
13
14 The thermal profile of the exposed membrane was observed using a 320×240 infrared thermal
15 imaging camera (Model HTI-19 with 300,000 Pixels). Bacteria from the membrane before and
16 after solar irradiation were collected by swabbing an inoculation loop across the surface.
17
18 Subsequently, the inoculation loops were streaked onto agar plated with LB medium and the
19 inoculated plates were incubated for 24 h to determine photothermal disinfection ability.
20
21
22
23
24
25
26
27
28
29
30
31
32
33
34
35
36
37

38 **2.6. Solar steam generation**

39
40
41 A bilayered rGO/BNC:BNC membrane with diameter and thickness of 5.1 cm and 1 mm
42 respectively was floated on the top of a glass beaker (5.3 cm diameter, 7.5 cm height and 2 mm
43 thickness) filled with deionized water. It was irradiated using a solar simulator with the intensity
44 of 0.6 KW/m^2 (one sun) for 60 min. The thermal profile was then monitored using an IR camera.
45
46 Steam generation experiments were carried out using the deionized water. The water evaporation
47 rate was evaluated by quantifying the weight loss of water per unit time per unit exposure area.
48
49
50
51
52
53
54
55
56
57
58
59
60

1
2
3 The difference in weight was assessed through an electronic weighing balance, having an accuracy
4 of 0.01 g.
5
6

7 8 **3. Results and discussion** 9

10 **3.1. Biosynthesis of bilayered hydrogels** 11

12
13
14 BNC biosynthesis occurs via two stages: (i) fast aerobic growth in the presence of excess carbon
15 substrate and oxygen; (ii) static growth following depletion of carbon and oxygen.^{16,21} In the
16 absence of GO, the resulting BNC was white, translucent, and flexible. BNC formation begins at
17 the air-liquid interface since it requires both oxygen and a carbon source. Once the entangled layer
18 of cellulose fibers starts to develop at the surface, growth continues ‘layer by layer’^{14,21} with
19 growth of subsequent layers occurring in the depth of the growth medium as oxygen diffuses
20 inwardly. This process results in the formation of a network of dense, 3-D structured, parallel-
21 oriented entangled layers of BNC. When GO is included within the growth medium, BNC grows
22 around the GO sheets leading to GO entanglement within the composite hydrogel. Adsorption of
23 GO to the slowly growing BNC layers ensured formation of a compact GO/BNC composite
24 hydrogel (i.e., single-layered GO/BNC).⁴⁷ GO/BNC hydrogels were synthesized by growing
25 *G. xylinus* in mixtures of nutrient medium modified with CSL and GO. To quantify how CSL
26 influences the formation of the GO/BNC hydrogel, the bacterial growth medium was modified
27 with varying amounts of CSL (0–80 mL CSL per L of standard nutrient medium) while
28 maintaining the GO concentration at 0.05 wt%. The BNC biosynthesis rate is dependent upon the
29 concentration of CSL growth enhancer substrate. CSL is a viscous soluble product formed as a by-
30 product of corn wet-milling. It is an excellent source of carbon and nitrogen as it contains various
31 amino acids, vitamins, and minerals.³⁸ CSL addition to the growth medium enhances *G. xylinus*
32 growth and the production of BNC.^{38,53,54} Modifications in the formation of a bilayer structured
33
34
35
36
37
38
39
40
41
42
43
44
45
46
47
48
49
50
51
52
53
54
55
56
57
58
59
60

1
2
3 GO embedded BNC hydrogels with varying quantities of supplemental CSL are illustrated in Fig.
4
5 1a. Photographic images representing front and back views with varying levels of incorporation of
6
7 GO within the BNC fibers depending on the CSL level are given in Fig. 1b. As expected, in the
8
9 absence of CSL, the BNC growth rate was quite low. When CSL was added to the growth medium
10
11 at ratios of 20-40 mL/L, the embedment of GO within the hydrogel resulted in production of two
12
13 distinct layers: 1) a pristine BNC layer, and 2) an adherent GO/BNC composite layer (i.e.,
14
15 bilayered GO/BNC:BNC) (Fig. 1c,e). Because the growth of *G. xylinus* is enhanced by CSL, it is
16
17 possible to produce a BNC layer at a rate that does not allow incorporation of GO during the initial
18
19 incubation stage. As incubation proceeds, depletion of the CSL occurs simultaneous to a decrease
20
21 in oxygen availability within the depth of the nutrient medium. This process reduces the BNC
22
23 production rate; hence GO has the opportunity to adsorb onto the growing surface. As *G. xylinus*
24
25 grows around the GO adsorbed BNC, a GO embedded BNC layer develops resulting in formation
26
27 of the bilayered hydrogel. When the CSL concentration exceeded 40 mL/L bilayer formation was
28
29 not observed. The BNC formed under these conditions was similar to that of pristine BNC since
30
31 there was minimal observed attachment of GO. Under these conditions GO weakly adsorbed to
32
33 the surface of BNC within the incubation period of 72 h, thus resulting in the formation of either
34
35 a poorly embedded GO/BNC layer or a pristine BNC layer. Photographic images illustrating the
36
37 minimal attachment of GO to the BNC fibers for CSL > 80 mL/L are shown in Fig. S1. A sufficient
38
39 quantity of GO is required to obtain perfectly stacked layers along with BNC fibers to achieve the
40
41 final desired membrane pore size, particle rejection, and water flux. The addition of GO to growth
42
43 medium was varied as 0.025, 0.05, and 0.075 wt% to a fixed volume of growth medium. As
44
45 illustrated in the supplementary material (Fig. S2), 0.05 and 0.075 wt% loading of GO was found
46
47 to be sufficient to fully cover the BNC layers, whereas 0.025 wt% was insufficient.
48
49
50
51
52
53
54
55
56
57
58
59
60

3.2. Membrane characterization

SEM analysis was performed to characterize rGO incorporation into the entangled BNC fibers as a function of varying concentrations of CSL and GO. Pristine BNC has a porous 3D structure composed of entangled nonwoven nanofibrils having cross-sectional diameters of >100 nm (Fig. 2a). Addition of GO in the absence of CSL resulted in production of a freeze-dried rGO/BNC membrane (M0) consisting of loosely packed rGO anchored BNC fibers within a 3D porous network (Fig. S3a). Cross-section SEM analysis of the M0 membrane shows that GO on BNC is anchored in a layered manner with a total thickness of ~ 200 μm (Fig. S2b). The rGO/BNC:BNC bilayered membrane (M1) synthesized in the presence of 20 mL/L CSL exhibited smooth, tightly packed, uniformly distributed rGO sheets anchored to the BNC nanofibrils (Fig. 2b,c). Cross-sectional confocal microscope images of the M1 membrane indicate a bilayered structure consisting of rGO/BNC as one layer followed by a pristine BNC layer and a total membrane thickness of ~ 1 mm (Fig. 2d). The bilayered membrane (M2) formed with 40 mL/L of CSL exhibits a network of heterogeneously intact rGO embedded within the BNC composite (Fig. S3c). The surface morphology of the M3 membrane developed in growth medium amended with 60 mL/L of CSL showed randomly anchored rGO flakes on the surface fibrils of the BNC layers. The fast-growing nature of the growth medium reduces attachment of GO flakes to the BNC fibers (Fig. S3d).

Raman analysis was performed to evaluate the quality of GO used in the hydrogels and rGO formed in the membranes. The typical characteristic features of the GO/rGO Raman spectrum are the graphite peak (G-band) and the defect peak (D-band; Fig. 2e). The G band of GO at 1596 cm^{-1} results from E_{2g} phonons at the Brillouin zone center corresponding to sp^2 carbon, while the D band at 1320 cm^{-1} reflects defects in the graphene sheets that reflect oxygen functional groups.⁵⁵

1
2
3 The intensity ratio of the D and G band (I_D/I_G) was found to decrease from 2.86 (GO) to 1.67
4 (rGO/BNC). The higher I_D/I_G of GO reflects defects introduced by the oxygen functional groups
5 to the graphitic chains. The considerable recovery of the conjugated graphitic framework upon the
6 de-functionalization of oxygen groups after sterilization and washing of GO/BNC hydrogel at
7 alkaline conditions resulted in the decreased I_D/I_G of the rGO/BNC membrane. XPS analysis was
8 carried out to further understand the extent of oxygen reduction during NaOH boiling. Survey
9 spectra of GO and the cleaned/dried bilayer membrane illustrate the reduction in the O1s signal
10 following NaOH treatment (Fig. 2f). High-resolution C1s spectra of GO indicate binding energy
11 configurations at 284 eV, 286.5 eV and 288.2 eV corresponding to sp^2 carbon (C=C) and oxidized
12 sp^3 carbon representing the C=O and C–O functional groups^{56,57} (Fig. 2g,h).

13
14
15
16
17
18
19
20
21
22
23
24
25
26
27 TGA analysis of the rGO/BNC (M0) and the rGO/BNC:BNC (M1 – M3) bilayer membranes was
28 done to understand the extent of attachment of the rGO sheets to BNC produced using different
29 growth medium compositions (Fig. 2i). No significant weight loss was observed at temperatures
30 <150 °C for all of the samples. Mass reductions of 2%, 4%, 6%, and 65% observed for the M0,
31 M1, M2, and M3 membranes at 350 °C reflect the degradation of cellulose into CO_2 and H_2O .
32 Additional reductions in weight were attributed to the decomposition of damaged graphitic carbon
33 backbones and cellulose residues at temperatures > 350 °C. Residual weights of 97% (M0), 96%
34 (M1), 93% (M2), and 58% (M3) observed for the corresponding membranes indicate a pattern of
35 increased weight loss for membranes as a function of the amount of BNC. A similar trend was
36 observed for bilayered membranes produced with different loadings of rGO (G1 – G3) (Fig. S4).
37 Bilayered membranes made with 0.025 wt% of GO showed 100% weight loss that could be
38 attributed to the complete decomposition of the cellulose and the damaged graphitic carbon
39 network. In the case of G1 (0.05 wt% GO) and G2 (0.075 wt% GO) bilayered rGO/BNC:BNC
40
41
42
43
44
45
46
47
48
49
50
51
52
53
54
55
56
57
58
59
60

1
2
3 membranes, residual weights of 97.8% and 93% were observed, respectively. The final weights
4 represent the presence of a thermally stable graphitic carbon framework in the rGO of
5 rGO/BNC:BNC membrane that regained its property during the boiling (cleaning step) of
6 GO/BNC:BNC hydrogel in NaOH.
7
8
9
10
11

12
13 Membrane stability was studied using ultrasonication at different pH conditions. Pieces of
14 bilayered rGO/BNC:BNC membranes were soaked in glass beakers containing acidic (pH 2.1),
15 neutral (pH 6.9) and alkaline solutions (pH 12.0) and ultra-sonicated for 3 h. The membranes were
16 found to be intact and stable after sonication at all pH values (Fig. S7).
17
18
19
20
21
22

23 **3.3. Particle rejection and water flux studies**

24
25
26 The particle rejection efficiency of the bilayered rGO/BNC:BNC membranes was tested using ≈ 21
27 nm AuNPs (Fig. 3a). BNC membranes without rGO (G0) and single-layered rGO/BNC (M1)
28 removed 13.9% and 29.3% of AuNPs, respectively. The M0 membrane encompassed of loosely
29 packed rGO layers entangled within BNC do not provide pore sizes less than ~ 20.6 nm. Similarly,
30 the low removal efficiency of AuNPs observed for the BNC membrane is a result of the fact that
31 the entangled BNC contains an insufficient quantity of fibers to effectively remove the
32 nanoparticles. The water flux of the M0 membrane was as high as $198.6 \text{ L h}^{-1} \text{ m}^{-2}$ and a water flux
33 too high to be measured was observed for BNC mainly because of its large membrane pore size
34 (Fig. 3b). In contrast, bilayered rGO/BNC:BNC membranes (M1 and M2) removed 100% and
35 96.0% of the AuNPs (~ 20.6 nm) and exhibited water fluxes of 146.3 and $104.5 \text{ L h}^{-1} \text{ m}^{-2}$,
36 respectively. Fig. 3c represents the UV spectra of the AuNPs (~ 20.6 nm) before and after filtration.
37
38
39
40
41
42
43
44
45
46
47
48
49
50
51
52
53
54
55
56
57
58
59
60

1
2
3 medium was 20 mL/L followed by that for the M2 membrane (=40 mL/L of CSL). In the case of
4 the M3 and M4 membranes, 99.8 and 100% removal of AuNPs were observed. While improved
5 rejection of AuNPs was observed for M3 and M4, they exhibited minimal water flux (73.2 L h^{-1}
6 m^{-2} for M3 and $15.7 \text{ L h}^{-1} \text{ m}^{-2}$ for M4).
7
8
9
10
11

12
13 The M1 membrane was tested for the removal of smaller AuNPs ($\sim 4.2 \text{ nm}$) to quantify the effective
14 pore size. Complete removal of AuNPs suggest that the rGO sheets were stacked along with the
15 BNC in a manner that resulted in a final effective pore size $< 4.2 \text{ nm}$ (Fig. 3f). The water flux of
16 M1 obtained at 30 psi pressure was comparable to a commercial ultrafiltration membrane (146.3
17 $\text{Lh}^{-1}\text{m}^{-2}$)⁵⁸. Although higher AuNP rejection was achieved with the M3 and M4 membranes, lower
18 water fluxes were observed. Rejection of AuNPs and water fluxes were compared for the
19 membranes produced with the varying loads of GO (G1 – G3). Complete removal of both 4.2 and
20 20.6 nm AuNPs by the G2 and G3 membranes with corresponding water fluxes of 146.3 and 123.5
21 $\text{Lh}^{-1}\text{m}^{-2}$ represent optimum performance. While G1 removed 98.5% of 20 nm AuNPs with a water
22 flux of $151.1 \text{ Lh}^{-1}\text{m}^{-2}$, suggesting that an insufficient amount of GO was entangled with BNC
23 (Fig. 3d,e). The removal efficiency of plasmid DNA through different membranes was studied
24 (G0, M1, M2, M3) (Fig. 3g). Complete removal (100%) of plasmid DNA was measured for all of
25 the membranes since the size of the ds DNA was measured to be $\sim 350 \text{ nm}$ as per DLS analysis
26 (Fig. 3h). Continuous monitoring of membrane (M1) over 180 min of run time resulted in the
27 insignificant variation in the measured water flux (Fig. 3i).
28
29
30
31
32
33
34
35
36
37
38
39
40
41
42
43
44
45
46
47

48 **3.4. Photothermal disinfection**

49
50
51 To quantify the photothermal disinfection capacity of the membranes, *E. coli* stocks ($\sim 2.0 \times 10^7$
52 CFU/mL) were filtered through the membranes and they were then exposed to solar irradiation for
53
54
55
56
57
58
59
60

1
2
3 10 min. Filtrate collected through the different membranes was analyzed to determine the removal
4 efficiency of *E. coli* (Fig. 4a,b). All of the rGO embedded BNC membranes filtered the bacteria
5 completely, whereas BNC alone showed a removal efficiency of 99.999%. The *E. coli* filtration
6 efficiency is dependent on the membrane pore size and rGO embedded BNC (G0, G1, G2, G3)
7 exhibit an appropriate pore size to exclude *E. coli* effectively. The ultrafiltration performance of
8 this biosynthesized membrane is comparable to other non-biodegradable polymeric membranes in
9 removing bacteria (Table S1). It is evident that rGO has considerable photothermal properties
10 under solar irradiation with the possibility to inactivate bacteria entrapped within the
11 rGO/BNC:BNC membranes. The degree of photothermal disinfection is dependent on the
12 magnitude of the local temperature rise and the duration of solar exposure.³³ The presence of
13 abundant π electrons within the sp^2 carbon of rGO results in narrow energy levels; thus, exhibiting
14 high light to heat conversion.^{2,59} When solar light irradiates the surface, the surface temperature of
15 rGO embedded BNC membranes increased from 24 °C to 40-45 °C within 30 s of exposure (Fig.
16 4c) and reached 55-70 °C following 10 min of continuous exposure. Whereas the GO membrane
17 reached up to 62 °C in 60 min of solar irradiation (Fig. S8c). The rate of temperature increase for
18 the BNC membrane was much less as it only reached 40 °C after 10 min. The temperature profile
19 of the bilayer rGO/BNC:BNC membrane exhibited two stages.⁶⁰ In the first stage, the temperature
20 plateaued within 10 and 25 min of exposure. During this stage, solar energy evaporates water
21 molecules entrapped within the rGO/BNC medium. In the second stage, solar energy further raised
22 the temperature until it attained equilibrium values of 83, 90.5, and 100 °C for bilayered
23 membranes G1, G2, and G3, respectively. The rate of increase in temperature was dependent on
24 the amount of rGO loaded on the BNC and follows the order: $G3 > G2 > G1$. Comparison of single
25 layer rGO/BNC and bilayer rGO/BNC:BNC shows that the temperature change was more rapid
26
27
28
29
30
31
32
33
34
35
36
37
38
39
40
41
42
43
44
45
46
47
48
49
50
51
52
53
54
55
56
57
58
59
60

1
2
3 for single layer relative to bilayer (Fig. 4d). However, there was no distinct two-stage temperature
4 profile observed for the single layer rGO/BNC membrane. Due to the minimal water entrapping
5 capacity of the single layer rGO/BNC membrane, solar energy is rapidly utilized to raise the
6 temperature with a higher water evaporation rate. A temperature range of 60-65 °C is sufficient to
7 inactivate *E. coli* through the denaturation of cellular enzymes/proteins and cell membrane damage
8 (Fig. 4e). Both single (0.05 wt% GO) and bilayer (0.05 and 0.075 wt% GO) rGO embedded BNC
9 membranes inactivated *E. coli* cells completely (100% removal), while insignificant inactivation
10 was observed with the BNC membrane. To understand the maximum rise in the temperatures of
11 the membranes (BNC, M0 and M1), the irradiation was carried out for 60 min (Fig. 4f). The
12 temperature of the BNC membrane reached only 39.3 °C while M1 and M2 membranes achieved
13 up to 92.3 and 96 °C respectively. Control experiments in the absence of sunlight indicate there is
14 no biocidal effect imposed by the rGO/BNC membrane over a contact period of 60 min and thus
15 the measured inactivation solely reflects photothermal effects.

3.5. Solar steam generation

34
35
36
37 The capacity of the bilayer rGO/BNC:BNC membranes (0.05 wt% GO) and the rGO/BNC (0.05
38 wt% GO) and pristine BNC membranes to generate steam under simulated solar light was
39 evaluated. Fig. 5a demonstrates rapid water evaporation at the air/water interface upon floating of
40 the bilayered membrane within the glass beaker. The steam generation efficiency of the membrane
41 was determined based on the measured weight loss of water due to evaporation as a function of
42 exposure area and irradiation time (Fig. 5b). Bilayer rGO/BNC:BNC membranes exhibited a water
43 evaporation rate of 1.96 kg m⁻² h⁻¹ for the M1 membrane. In contrast, the BNC membrane alone
44 and water without any membranes resulted in measured evaporation rates of only 0.6 and 0.47 kg
45 m⁻² h⁻¹, respectively. The temperature of the M1 membrane reached 56.9 °C in 60 min whereas the

1
2
3 water surface without the membrane reached only 32 °C (Fig. 5c). Bilayer membrane exhibited a
4
5 3.26 times greater evaporation rate than pristine BNC. The bilayer rGO/BNC:BNC membrane was
6
7 reused 4 times, and constant evaporation rates were achieved without much variation thus
8
9 indicating that the membrane is highly stable and reusable. The water evaporation rate of bilayer
10
11 rGO/BNC: BNC (M1) membrane was 1.20 times higher than the rGO/BNC (M0) membrane (1.64
12
13 kg m⁻²h⁻¹). This value reflects the importance of the bilayered membrane to facilitate water
14
15 evaporation. The presence of rGO in the rGO/BNC layer enhances absorption of incident light and
16
17 photothermal conversion of absorbed light into heat. Properties of BNC such as its porous nature
18
19 and hydrophobicity enable the rapid transport of water molecules from the bulk liquid phase to the
20
21 evaporative membrane surface (i.e., the light exposure layer of rGO/BNC).⁶¹ The low thermal
22
23 conductive property of the BNC could also prevent heat loss to the bulk liquid.⁶²
24
25
26
27
28

29 The variation in temperature of the bilayered membrane (M1) floated at the air/liquid interface
30
31 was captured using an IR camera. Upon solar light irradiation, the temperature rapidly increased
32
33 to 38.9 °C from 25 °C within 30 s of exposure (Fig. 5d), while the temperature reached 48.3°C
34
35 after 5 min and 52.3 °C after 15 min (Fig. 5e,f). Due to the continuous exposure to simulated solar
36
37 light, the surface temperature of the bilayered membrane reached 54 °C in 30 min and 56.2 °C in
38
39 45 min with a slow rate (Fig. 5g,h). A further change in temperature was not apparent and attained
40
41 equilibrium upon extended exposure to irradiation. The rapid rise in the temperature is due to the
42
43 combined properties of rGO and BNC. High absorption and manifold scattering of the incident
44
45 light by rGO and BNC fibers respectively increase the optical path length and expand its absorption
46
47 resulting in high heat conversion.^{21,63} Performance of this biosynthesized photothermal foam
48
49 towards steam generation is comparable to other GO/rGO based polymeric membranes/foams
50
51 (Table S2).
52
53
54
55
56
57
58
59
60

4. Conclusions

This study illustrates the simple and novel one-step biosynthesis of a versatile bilayer GO embedded BNC hydrogel through an environmentally friendly approach. We found that the adsorption and incorporation of GO sheets onto the BNC fibers of the bilayered hydrogel can be controlled by varying the growth rates of the BNC and can be significantly manipulated by supplementation of CSL growth enhancer compounds to the nutrient growth medium. Biosynthesis of the bilayer hydrogel occurs in two stages. In the initial stage of hydrogel biosynthesis, the pristine BNC layer forms due to the fast growth rate and the minimal attachment of GO sheets. In the second stage, depletion of substrates (carbon and oxygen) reduce the growth rate of BNC, thus enhancing adsorption and incorporation of GO into the BNC. The optimized moderate thickness of bilayer rGO/BNC:BNC membrane allowed us to explore its versatile application for water purification, including particle filtration, photothermal disinfection of entrapped bacteria, and solar steam generation processes. The bilayered membrane exhibited high stability under variable mechanical and chemical environments and exhibits a high degree of reusability as indicated by water flux measurements (for M1: decreasing only from 145 to 130 L h⁻¹m⁻² following filtration of *E. coli* and ultrasonic cleaning). This biobased membrane is environmentally benign relative to synthetic and metal incorporated membranes. Moreover, the simple and non-toxic biosynthesis approach demonstrated in this study can also find utility for the production of a variety of functional nanocomposites containing alternative 2D materials. Such nanocomposites will be useful for applications in catalysis, sensors, drug delivery, energy harvesting and storage.

1
2
3 **Supporting information**
4
5

6 Photographic images of hydrogels obtained with different supplementations of CSL and GO; SEM
7 morphology and TGA of membranes; Size distribution of AuNPs obtained using DLS; Calibration
8 curves of AuNPs; Membrane stability study under ultrasonication with different pH solutions;
9 SEM, TGA and photothermal properties of GO
10
11
12
13
14
15

16 **Conflicts of interest**
17
18

19 The authors declare no competing financial interest.
20
21
22
23
24
25
26
27
28
29
30
31
32
33
34
35
36
37
38
39
40
41
42
43
44
45
46
47
48
49
50
51
52
53
54
55
56
57
58
59
60

Reference

- 1 Y. Lin, H. Xu, X. Shan, Y. Di, A. Zhao, Y. Hu and Z. Gan, *J. Mater. Chem. A*, 2019, **7**, 19203–19227.
- 2 Y. S. Jun, X. Wu, D. Ghim, Q. Jiang, S. Cao and S. Singamaneni, *Acc. Chem. Res.*, 2019, **52**, 1215–1225.
- 3 C. Zhang, H. Q. Liang, Z. K. Xu and Z. Wang, *Adv. Sci.*, , DOI:10.1002/advs.201900883.
- 4 X. Song, Y. Wang, C. Wang, M. Huang, S. Gul and H. Jiang, *ACS Sustain. Chem. Eng.*, 2019, **7**, 4889–4896.
- 5 L. Shi, Y. Shi, C. Zhang, S. Zhuo, W. Wang, R. Li and P. Wang, *Energy Technol.*, 2020, **2000456**, 1–10.
- 6 V. Nair, M. J. Muñoz-Batista, M. Fernández-García, R. Luque and J. C. Colmenares, *ChemSusChem*, 2019, **12**, 2098–2116.
- 7 D. Hao, Y. Yang, B. Xu and Z. Cai, *ACS Sustain. Chem. Eng.*, 2018, **6**, 10789–10797.
- 8 L. Noureen, Z. Xie, Y. Gao, M. Li, M. Hussain, K. Wang, L. Zhang and J. Zhu, *ACS Appl. Mater. Interfaces*, 2020, **12**, 6343–6350.
- 9 X. Yang, Y. Yang, L. Fu, M. Zou, Z. Li, A. Cao and Q. Yuan, *Adv. Funct. Mater.*, 2018, **28**, 1–9.
- 10 J. Wang, Y. Li, L. Deng, N. Wei, Y. Weng, S. Dong, D. Qi, J. Qiu, X. Chen and T. Wu, *Adv. Mater.*, 2017, **29**, 1–6.
- 11 Q. Wang, L. Qiu, Y. Jia, Y. Chang, X. Tan, L. Yang and H. Chen, *Sol. Energy Mater. Sol. Cells*, 2019, **202**, 110116.
- 12 X. J. Zha, X. Zhao, J. H. Pu, L. S. Tang, K. Ke, R. Y. Bao, L. Bai, Z. Y. Liu, M. B. Yang and W. Yang, *ACS Appl. Mater. Interfaces*, 2019, **11**, 36589–36597.
- 13 W. Xu, X. Hu, S. Zhuang, Y. Wang, X. Li, L. Zhou, S. Zhu and J. Zhu, *Adv. Energy Mater.*, , DOI:10.1002/aenm.201702884.
- 14 Q. Jiang, D. Ghim, S. Cao, S. Tadepalli, K. K. Liu, H. Kwon, J. Luan, Y. Min, Y. S. Jun and S. Singamaneni, *Environ. Sci. Technol.*, 2019, **53**, 412–421.

- 1
2
3 15 Y. Wang, C. Wang, X. Song, S. K. Megarajan and H. Jiang, *J. Mater. Chem. A*, 2018, **6**,
4 963–971.
5
6 16 Q. Jiang, H. Gholami Derami, D. Ghim, S. Cao, Y. S. Jun and S. Singamaneni, *J. Mater.*
7 *Chem. A*, 2017, **5**, 18397–18402.
8
9 17 Y. Wang, C. Wang, X. Song, M. Huang, S. K. Megarajan, S. F. Shaikat and H. Jiang, *J.*
10 *Mater. Chem. A*, 2018, **6**, 9874–9881.
11
12 18 Z. Xie, Y. P. Peng, L. Yu, C. Xing, M. Qiu, J. Hu and H. Zhang, *Sol. RRL*, 2020, **4**, 1–28.
13
14 19 G. Liu, J. Xu and K. Wang, *Nano Energy*, 2017, **41**, 269–284.
15
16 20 P. Wang, *Environ. Sci. Nano*, 2018, **5**, 1078–1089.
17
18 21 Q. Jiang, L. Tian, K. K. Liu, S. Tadepalli, R. Raliya, P. Biswas, R. R. Naik and S.
19 Singamaneni, *Adv. Mater.*, 2016, **28**, 9400–9407.
20
21 22 F. Perreault, A. Fonseca De Faria and M. Elimelech, *Chem. Soc. Rev.*, 2015, **44**, 5861–
22 5896.
23
24 23 C. N. Yeh, K. Raidongia, J. Shao, Q. H. Yang and J. Huang, *Nat. Chem.*, 2015, **7**, 166–
25 170.
26
27 24 Y. Jiang, Q. Zeng, P. Biswas and J. D. Fortner, *J. Memb. Sci.*, 2019, **581**, 453–461.
28
29 25 M. Z. Fahmi, M. Wathoniyyah, M. Khasanah, Y. Rahardjo, S. Wafiroh and Abdulloh,
30 *RSC Adv.*, 2018, **8**, 931–937.
31
32 26 F. Guo, C. Zhang, Q. Wang, W. Hu, J. Cao, J. Yao, L. Jiang and Z. Wu, *J. Appl. Polym.*
33 *Sci.*, 2019, **136**, 28–30.
34
35 27 X. Zhou, F. Zhao, Y. Guo, Y. Zhang and G. Yu, *Energy Environ. Sci.*, 2018, **11**, 1985–
36 1992.
37
38 28 Y. Wang, Z. Zhang, T. Li, P. Ma, H. Zhang, M. Chen, M. Du and W. Dong, *ACS Appl.*
39 *Mater. Interfaces*, 2019, **11**, 44886–44893.
40
41 29 Z. Xie, Y. Duo, Z. Lin, T. Fan, C. Xing, L. Yu, R. Wang, M. Qiu, Y. Zhang, Y. Zhao, X.
42 Yan and H. Zhang, *Adv. Sci.*, , DOI:10.1002/advs.201902236.
43
44 30 J. C. Del Río, J. Rencoret, A. Gutiérrez, T. Elder, H. Kim and J. Ralph, *ACS Sustain.*
45 *Chem. Eng.*, 2020, **8**, 4997–5012.
46
47 31 S. Sun, S. Sun, X. Cao and R. Sun, *Bioresour. Technol.*, 2016, **199**, 49–58.
48
49 32 X. Wu, L. Wu, J. Tan, G. Y. Chen, G. Owens and H. Xu, *J. Mater. Chem. A*, 2018, **6**,
50 12267–12274.
51
52 33 K. Liu, Q. Jiang, S. Tadepalli, R. Raliya, P. Biswas, R. R. Naik and S. Singamaneni, *ACS*
53 *Appl. Mater. Interfaces*, 2017, **9**, 7675–7681.
54
55
56
57
58
59
60

- 1
2
3 34 H. Liu, C. Chen, G. Chen, Y. Kuang, X. Zhao, J. Song, C. Jia, X. Xu, E. Hitz, H. Xie, S.
4 Wang, F. Jiang, T. Li, Y. Li, A. Gong, R. Yang, S. Das and L. Hu, *Adv. Energy Mater.*, ,
5 DOI:10.1002/aenm.201701616.
6
7 35 Z. Li, C. Wang, T. Lei, H. Ma, J. Su, S. Ling and W. Wang, *Adv. Sustain. Syst.*, 2019, **3**,
8 1800144.
9
10 36 H. Wei, K. Rodriguez, S. Renneckar, W. Leng and P. J. Vikesland, *Analyst*, 2015, **140**,
11 5640–5649.
12
13 37 S. Kang, A. Rahman, E. Boeding and P. J. Vikesland, *Analyst*, 2020, **145**, 4358–4368.
14
15 38 A. F. S. Costa, F. C. G. Almeida, G. M. Vinhas and L. A. Sarubbo, *Front. Microbiol.*,
16 2017, **8**, 1–12.
17
18 39 A. Sharma, M. Thakur, M. Bhattacharya, T. Mandal and S. Goswami, *Biotechnol.*
19 *Reports*, 2019, **21**, e00316.
20
21 40 A. F. Jozala, L. C. de Lencastre-Novae, A. M. Lopes, V. de Carvalho Santos-Ebinuma, P.
22 G. Mazzola, A. Pessoa-Jr, D. Grotto, M. Gerenutti and M. V. Chaud, *Appl. Microbiol.*
23 *Biotechnol.*, 2016, **100**, 2063–2072.
24
25 41 H. Gao, Q. Sun, Z. Han, J. Li, B. Liao, L. Hu, J. Huang, C. Zou, C. Jia, J. Huang, Z.
26 Chang, D. Jiang and M. Jin, *Carbohydr. Polym.*, 2020, **227**, 115323.
27
28 42 H. Luo, J. Dong, F. Yao, Z. Yang, W. Li, J. Wang, X. Xu, J. Hu and Y. Wan, *Nano-Micro*
29 *Lett.*, 2018, **10**, 1–10.
30
31 43 Q. Fang, X. Zhou, W. Deng, Z. Zheng and Z. Liu, *Sci. Rep.*, 2016, **6**, 1–11.
32
33 44 P. Liu, C. Zhu and A. P. Mathew, *J. Hazard. Mater.*, 2019, **371**, 484–493.
34
35 45 P. Dhar, J. Etula and S. B. Bankar, *ACS Appl. Bio Mater.*, 2019, **2**, 4052–4066.
36
37 46 H. Si, H. Luo, G. Xiong, Z. Yang, S. R. Raman, R. Guo and Y. Wan, *Macromol. Rapid*
38 *Commun.*, 2014, **35**, 1706–1711.
39
40 47 A. G. Nandgaonkar, Q. Wang, K. Fu, W. E. Krause, Q. Wei, R. Gorga and L. A. Lucia,
41 *Green Chem.*, 2014, **16**, 3195–3201.
42
43 48 W. Zhu, W. Li, Y. He and T. Duan, *Appl. Surf. Sci.*, 2015, **338**, 22–26.
44
45 49 L. Urbina, A. Eceiza, N. Gabilondo, M. Á. Corcuera and A. Retegi, *Int. J. Biol.*
46 *Macromol.*, 2020, **163**, 1249–1260.
47
48 50 P. Dhar, J. Etula and S. B. Bankar, *ACS Appl. Bio Mater.*, 2019, **2**, 4052–4066.
49
50 51 W. Leng, P. Pati and P. J. Vikesland, *Environ. Sci. Nano*, 2015, **2**, 440–453.
51
52 52 M. V. Riquelme Breazeal, J. T. Novak, P. J. Vikesland and A. Pruden, *Water Res.*, 2013,
53 **47**, 130–140.
54
55
56
57
58
59
60

- 1
2
3 53 P. Cerrutti, P. Roldán, R. M. García, M. A. Galvagno, A. Vázquez and M. L. Foresti, *J.*
4 *Appl. Polym. Sci.*, 2016, **133**, 1–9.
5
6 54 H. E. Kennedy, M. L. Speck and L. W. AURAND, *J. Bacteriol.*, 1955, **70**, 70–77.
7
8 55 G. Divyapriya, R. Srinivasan, I. M. Nambi and J. Senthilnathan, *Electrochim. Acta*, 2018,
9 **283**, 858–870.
10
11 56 G. Divyapriya, I. M. Nambi and J. Senthilnathan, *Chemosphere*, 2018, **209**, 113–123.
12
13 57 G. Divyapriya, I. M. Nambi and J. Senthilnathan, *Chem. Eng. J.*, 2017, **316**, 964–977.
14
15 58 R. Singh, in *Membrane Technology and Engineering for Water Purification*, 2015, pp. 1–
16 80.
17
18 59 D. P. Storer, J. L. Phelps, X. Wu, G. Owens, N. I. Khan and H. Xu, *ACS Appl. Mater.*
19 *Interfaces*, 2020, **12**, 15279–15287.
20
21 60 D. Li, Q. Zhao, S. Zhang, F. Wu, X. Yu, Z. Xiong, W. Ma, D. Wang, X. Zhang and B.
22 Xing, *Environ. Sci. Nano*, 2019, **6**, 2977–2985.
23
24 61 X. Li, G. Ni, T. Cooper, N. Xu, J. Li, L. Zhou, X. Hu, B. Zhu, P. Yao and J. Zhu, *Joule*,
25 2019, **3**, 1798–1803.
26
27 62 K. Uetani and K. Hatori, *Sci. Technol. Adv. Mater.*, 2017, **18**, 877–892.
28
29 63 Y. Yang, R. Zhao, T. Zhang, K. Zhao, P. Xiao, Y. Ma, P. M. Ajayan, G. Shi and Y. Chen,
30 *ACS Nano*, 2018, **12**, 829–835.
31
32
33
34
35
36
37
38
39
40
41
42
43
44
45
46
47
48
49
50
51
52
53
54
55
56
57
58
59
60

Figures and its legends

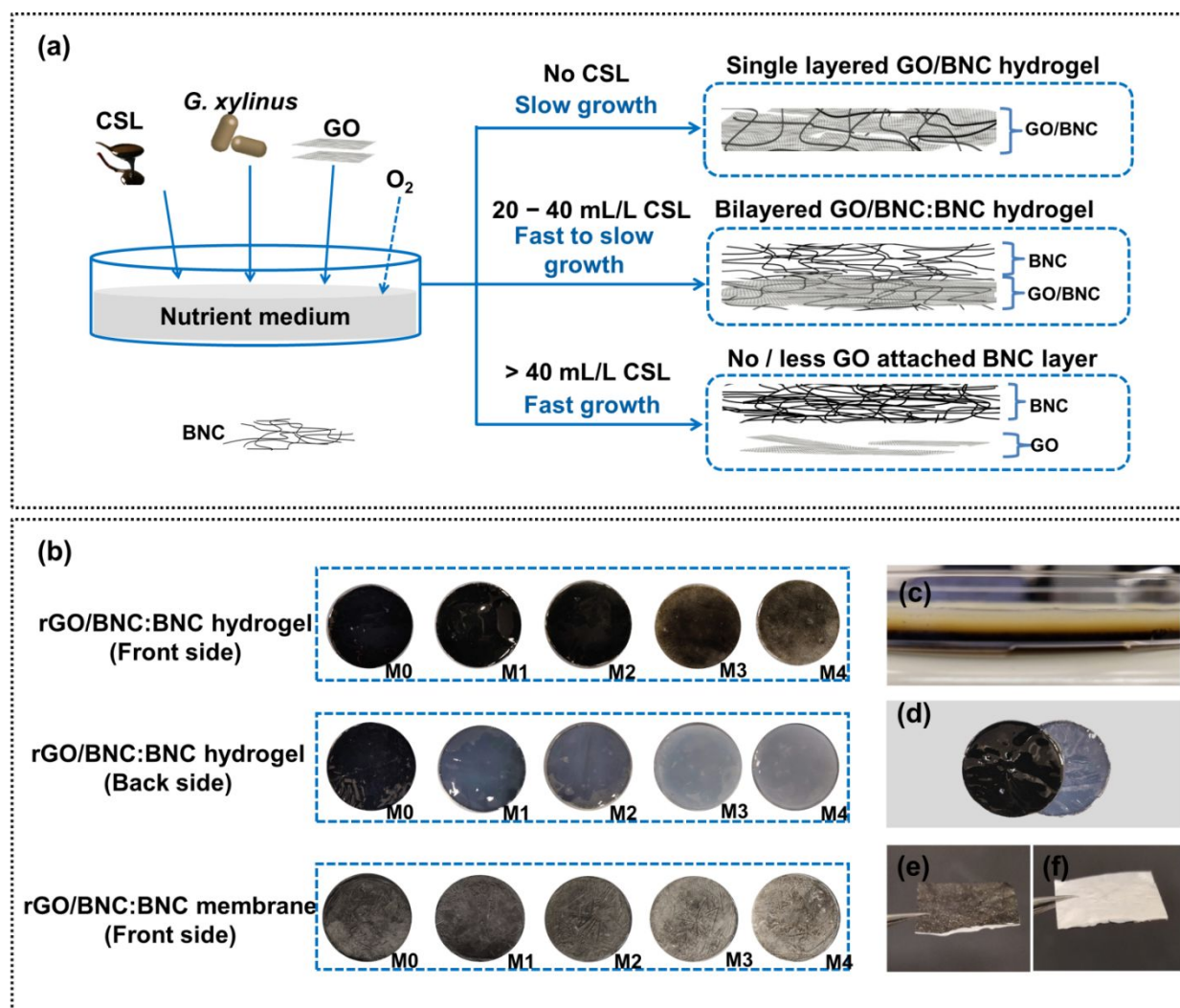


Fig. 1. (a) Schematic illustration representing the influence of CSL on the biosynthesis of GO/BNC and GO/BNC:BNC hydrogels, (b) Photographic images of rGO/BNC:BNC hydrogels (front and back surfaces) and membranes (front surface) representing the variation in the embedding of GO onto the entangled BNC fibers, Photographic image of (c) uncleaned GO/BNC:BNC hydrogels

representing the intersection, (d) cleaned rGO/BNC:BNC hydrogels, (e) and (f) rGO/BNC:BNC membrane (front and back surface)

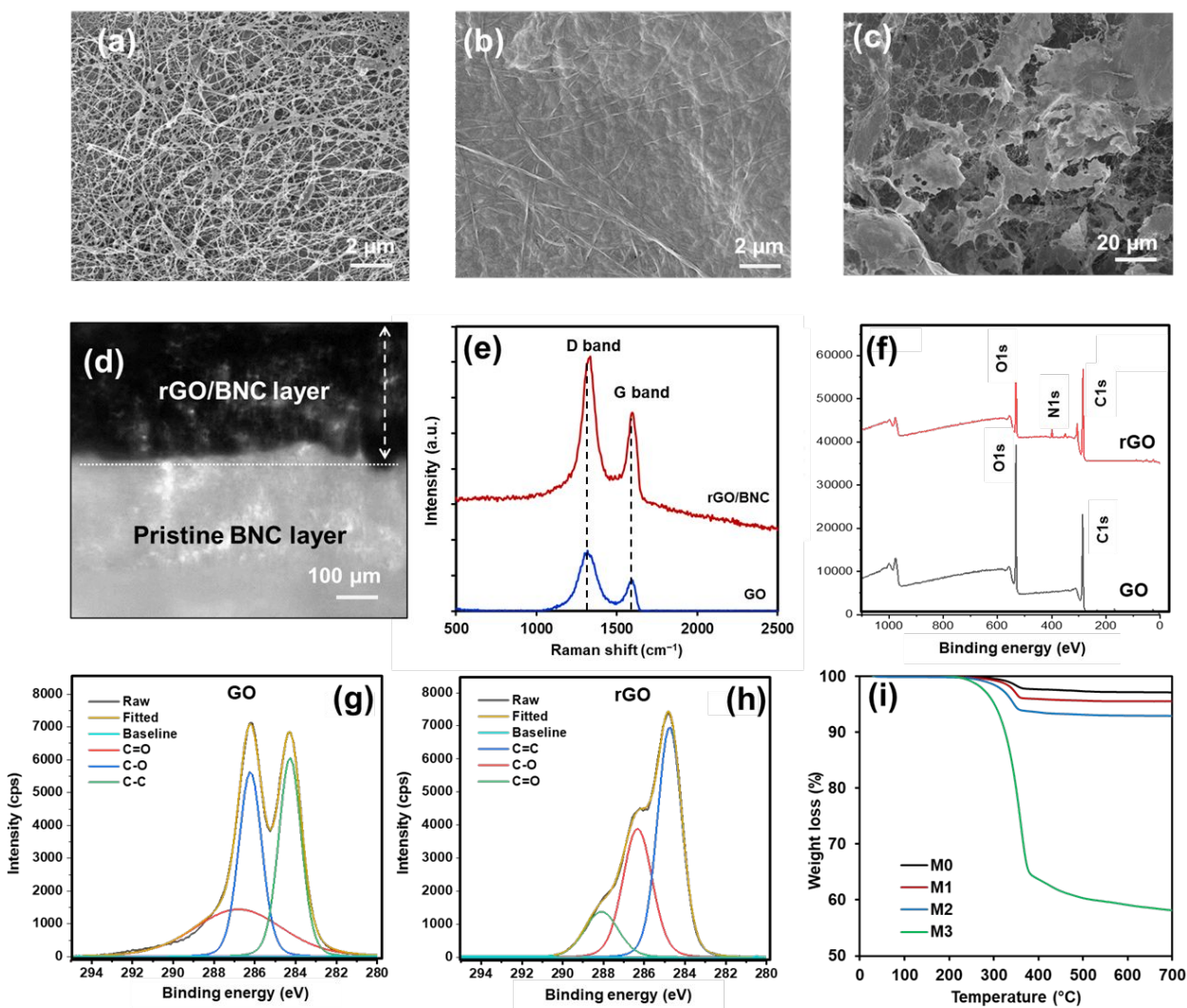


Fig. 2. SEM surface morphology of (a) BNC, (b) rGO/BNC:BNC membrane (low magnification), (c) rGO/BNC:BNC (high magnification) membrane (d) Cross section image of bilayer rGO/BNC:BNC membrane, (e) Raman spectrum of GO and rGO/BNC (M1), (f) XPS survey scans of pristine GO and rGO/BNC:BNC membrane, (g) C1s high resolution spectra of GO, (h) C1s high resolution spectra of rGO, and (i) TGA analysis of membranes M0 – M3

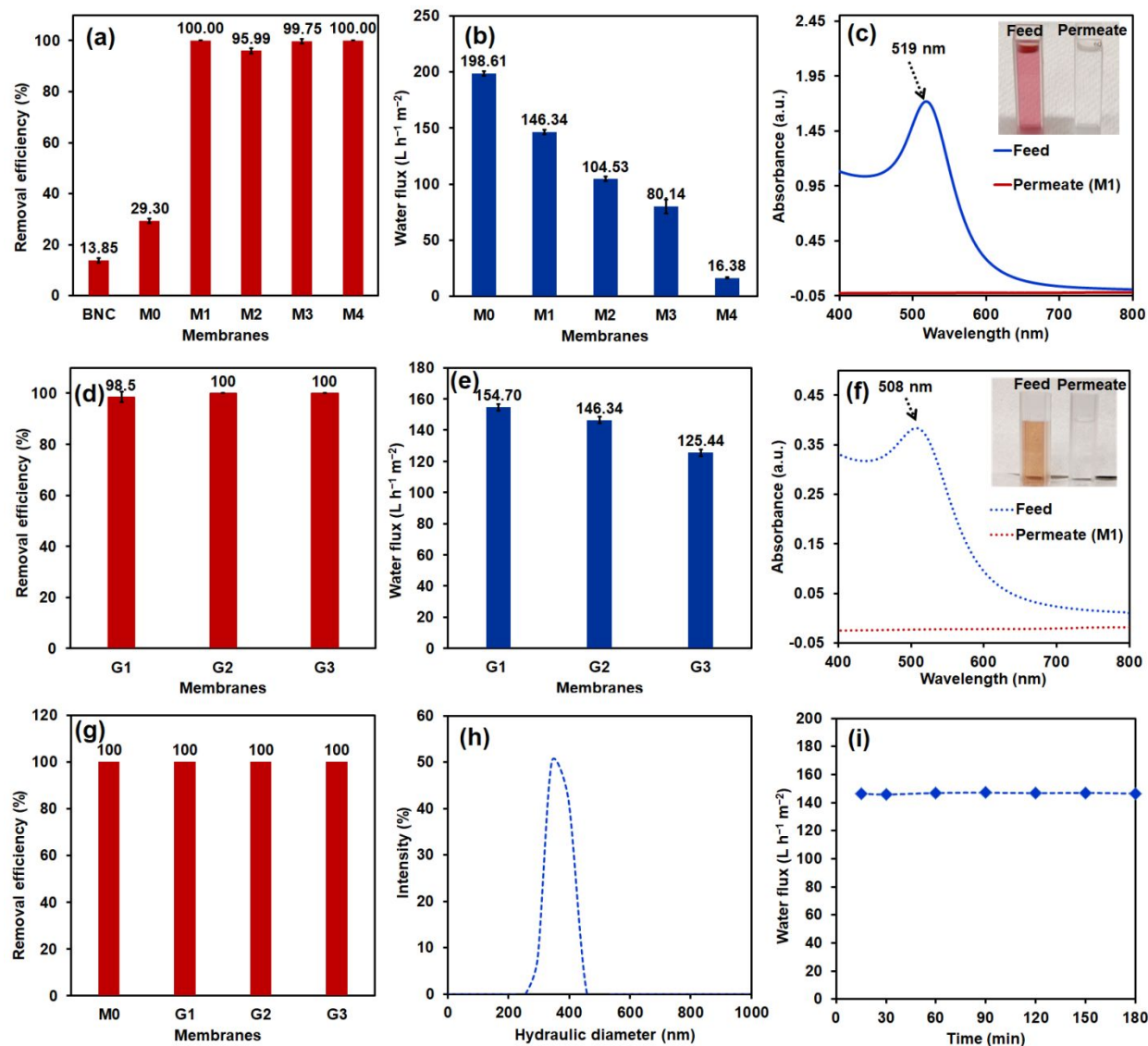


Fig. 3. (a) Removal efficiency of AuNPs (average diameter of 20.6 nm) at different membranes (BNC, M0 – M4) in dead-end filtration setup, (b) Water fluxes of different membranes (BNC, M0 – M4), (c) UV-Vis spectra of AuNPs (average diameter of 20.6 nm) representing the rejection efficiency in M1 membrane, (d) Removal efficiency of AuNPs (average diameter of 20.6 nm) at G1, G2 and G3 membranes (e) Water fluxes of G1, G2 and G3 membranes (BNC, M0 – M4), (f) UV-Vis spectra of AuNPs (average diameter of 4.2 nm) representing the rejection efficiency in M1 membrane, (g) Filtration removal of ds plasmid DNA extracted from *E. coli*, (h) DLS analysis of ds plasmid DNA, and (i) Variation in the water flux of membrane (M1) in the run time of 180 min.

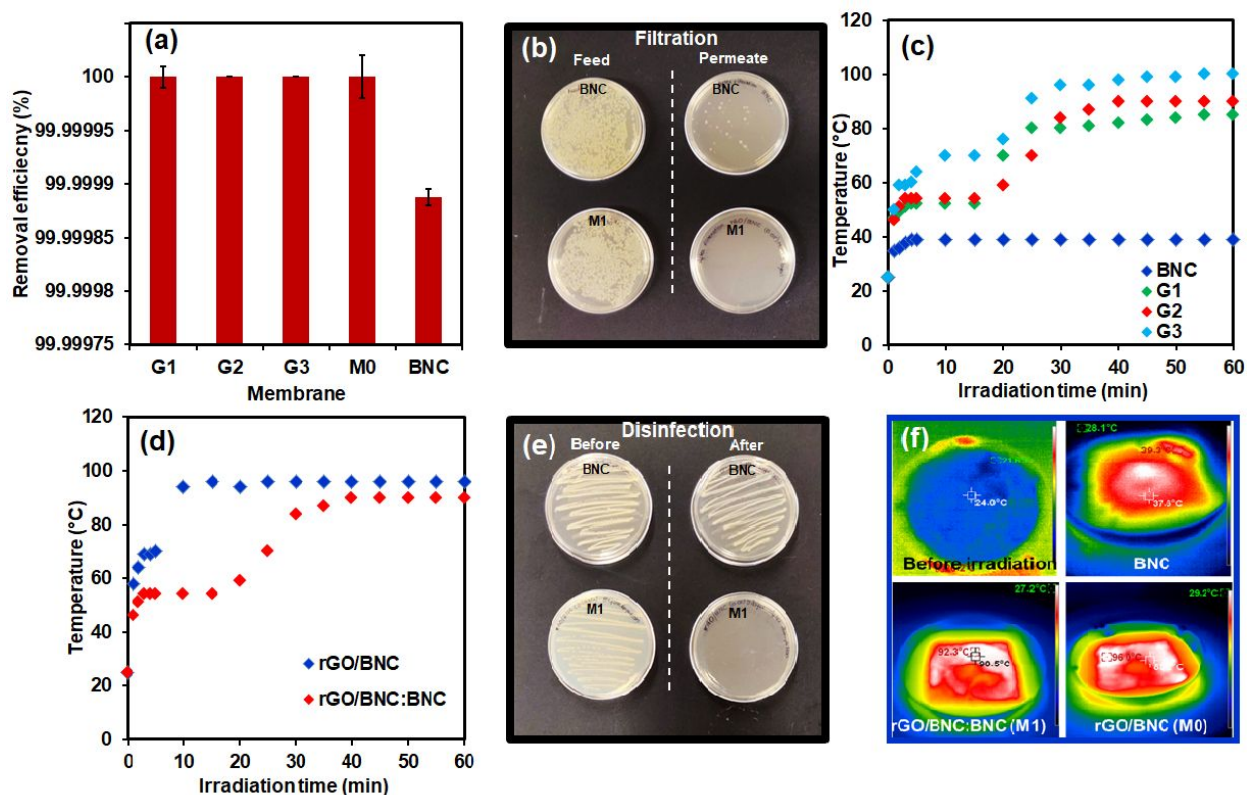


Fig. 4. (a) Filtration removal of *E. coli* at different membranes (BNC, M0, G1 – G3), (b) Photographic images representing the colonies formation of Feed and permeate, (c) temperature profiles of rGO/BNC:BNC and BNC membranes and water during the solar irradiation, (d) temperature profiles of rGO/BNC (0.05 wt/v%) and rGO/BNC:BNC (0.05 wt/v%) during the solar irradiation, (e) Bactericidal ability of photothermal membranes represented by streak plating method and (f) IR images representing the temperature variations of membranes (BNC, M0 and M1)

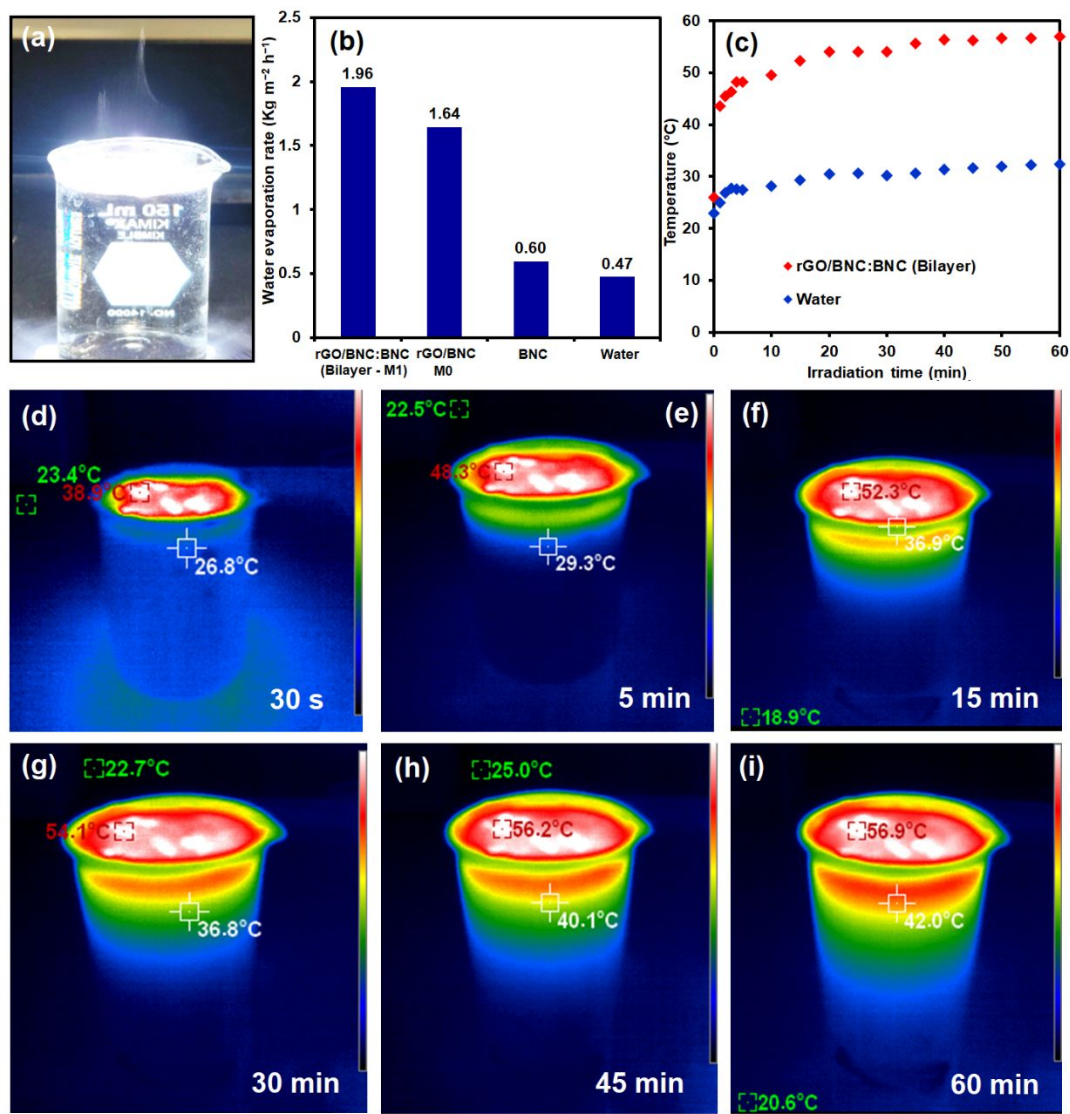


Fig. 5. (a) Photographic image representing steam generation on bilayered rGO/BNC:BNC – M1 membrane, (b) water evaporation rates of BNC, rGO/BNC and rGO/BNC:BNC membranes, (c – i) IR camera images representing the temperature changes at the air-liquid interface of rGO/BNC:BNC membrane under the solar irradiation with different time intervals